

Ground-state phase diagram of the repulsive fermionic $t - t'$ Hubbard model on the square lattice from weak coupling

Fedor Šimkovic, IV,¹ Xuan-Wen Liu,² Youjin Deng,² and Evgeny Kozik¹

¹*Department of Physics, King's College London, Strand, London WC2R 2LS, United Kingdom*

²*Hefei National Laboratory for Physical Sciences at Microscale, Department of Modern Physics, and Synergetic Innovation Center of Quantum Information and Quantum Physics, University of Science and Technology of China, Hefei, Anhui 230026, China*

(Received 14 December 2015; revised manuscript received 1 July 2016; published 5 August 2016)

We obtain a complete and numerically exact in the weak-coupling limit ($U \rightarrow 0$) ground-state phase diagram of the repulsive fermionic Hubbard model on the square lattice for filling factors $0 < n < 2$ and next-nearest-neighbor hopping amplitudes $0 \leq t' \leq 0.5$. Phases are distinguished by the symmetry and the number of nodes of the superfluid order parameter. The phase diagram is richer than may be expected and typically features states with a high—higher than that of the fundamental mode of the corresponding irreducible representation—number of nodes. The effective coupling strength in the Cooper channel λ , which determines the critical temperature T_c of the superfluid transition, is calculated in the whole parameter space and regions with high values of λ are identified. It is shown that besides the expected increase of λ near the Van Hove singularity line, joining the ferromagnetic and antiferromagnetic points, another region with high values of λ can be found at quarter filling and $t' = 0.5$ due to the presence of a line of nesting at $t' \geq 0.5$. The results can serve as benchmarks for controlled nonperturbative methods and guide the ongoing search for high- T_c superconductivity in the Hubbard model.

DOI: [10.1103/PhysRevB.94.085106](https://doi.org/10.1103/PhysRevB.94.085106)

I. INTRODUCTION

The repulsive Hubbard model [1,2]

$$H = -t \sum_{\langle i,j \rangle, \sigma} \hat{c}_{i\sigma}^\dagger \hat{c}_{j\sigma} + t' \sum_{\langle\langle i,j \rangle\rangle, \sigma} \hat{c}_{i\sigma}^\dagger \hat{c}_{j\sigma} + U \sum_i \hat{n}_{i\uparrow} \hat{n}_{i\downarrow} - \mu \sum_{i,\sigma} \hat{n}_{i\sigma}, \quad (1)$$

where $\hat{c}_{i\sigma}^\dagger$ creates a fermion with spin $\sigma = \{\uparrow, \downarrow\}$ on the lattice site i , $\hat{n}_{i\sigma} = \hat{c}_{i\sigma}^\dagger \hat{c}_{i\sigma}$, $\langle \dots \rangle$ and $\langle\langle \dots \rangle\rangle$ denote summation over nearest and next nearest neighbors, respectively, t and t' are the hopping amplitudes, U the on-site repulsion, and μ the chemical potential, is widely regarded as paradigmatic for strongly correlated electrons [3–7]. It is expected to capture a variety of intriguing macroscopic quantum phenomena, including, e.g., Mott-insulator physics, antiferromagnetism, striped phases, itinerant ferromagnetism, and high-temperature superconductivity. Due to recent remarkable progress in experimental technique, the Hubbard model can now be reliably emulated by ultracold atoms in optical lattices [8–14] and probed with unprecedented control, which in principle allows us to determine its phase diagram experimentally.

On the theoretical side, the model can be solved exactly in one dimension [15,16]. Already in 2D, more relevant in the context of condensed matter systems, obtaining the phase diagram for generic filling factors n and values of the interaction U remains a prohibitively complex problem. Since the seminal work by Kohn and Luttinger [17], who showed that the Cooper instability can develop even with repulsive interactions between fermions, a number of important results, exact in the weak-coupling limit ($U \rightarrow 0$), have been obtained by perturbative approaches. Baranov and Kagan [18–20] studied the Hubbard model in the dilute limit ($n \rightarrow 0$) by second-order perturbation theory. This work has been extended to the third order by Chubukov and Lu [21,22] and later

by Fukazawa *et al.* [23], which allowed us, in particular, to obtain the boundary between different superfluid phases in the limit $n \rightarrow 0$, $U \rightarrow 0$. The first weak-coupling phase diagram in the $n - t'$ plane for the range of parameters $0 \leq t' \leq 0.5$ and $0.25 \leq n \leq 0.75$ was obtained by Hlubina [24], and the effective coupling strengths for lines of $t' = 0$ and $t' = 0.3$ and $0 < n < 2$ were analyzed by Raghu *et al.* [25] (although, as we discuss below, with algebraic mistakes that are critical for final conclusions). Of special interest is the interplay of various ordered phases when the Fermi surface is tuned to the Van Hove singularity, or in the vicinity thereof. This competition of instabilities has been inspected mainly by different renormalization group techniques [26–33] at weak coupling [6,34–44] as well as in the strong-coupling regime [45–53].

Very recently, the phase diagram of the Hubbard model in a wide range of parameters was studied within the random phase approximation [54], which in principle is controlled in the $U \rightarrow 0$ limit. The approach however assumed the effective coupling in the Cooper channel λ to be fixed while the value of U was adjusted accordingly, so that the resulting phase diagram cannot be directly related to results in the $U \rightarrow 0$ limit. A number of previous works applied the weak-coupling approach to the Hubbard model but evaluated the observables at strong interactions [55–59]. Although meant to provide insight into the physics of strong correlations, such results are *a priori* uncontrolled and typically deviate significantly, even qualitatively, from the (numerically) exact solution in the correlated regime whenever the latter is available [60]. Accurate studies of the Hubbard model in the correlated regime have been possible by means of various Monte Carlo methods at half filling [61–63], where the notorious fermionic sign problem is absent, and, more recently, with the development of advanced numerical technique, at nonzero doping values [60,64–68]. Nonetheless, achieving full control over systematic errors in numerical studies of the doped Hubbard model in the correlated regime is still a very difficult problem [67], and a reliable phase diagram at nonzero values

of U is currently available only in a very limited region of the parameter space [60]. In the context of ongoing development and testing of new numeric techniques for the Hubbard model at strong correlations, accurate results in limiting cases are indispensable.

However, even in the weak-coupling limit $U \rightarrow 0$ a complete phase diagram in the full range of filling factors $0 < n < 2$ and most relevant next-nearest-neighbor hopping amplitudes $0 \leq t' \leq 0.5$ is still missing. Moreover, recent results in this parameter range [24,25] are in conflict with each other. A detailed analysis of the nodal structure of the Cooper-pairing order parameter for each symmetry sector in the phase diagram has not yet been carried out. Furthermore, in the context of high-temperature superconductivity, it would be of significant importance to identify regions of the phase diagram where the effective coupling strength is highest. Our paper is aimed at addressing all these issues.

We report the numerically exact in the limit $U \rightarrow 0$ ground-state phase diagram of the Hubbard model on the square lattice in the range of $0 \leq t' \leq 0.5$ and $0 < n < 2$. Our method consists of semianalytical treatment of the weak Cooper instability developing in the Landau Fermi liquid (FL) at temperatures much (exponentially) smaller than the Fermi energy E_F . We identify twelve different superconducting phases, differentiated by the number of nodes of the superfluid order parameter, with every allowed symmetry of the order parameter represented and study how the shape of the order parameter transforms across the boundaries between the phases in the parameter space. We perform an analysis of the effective coupling strength and identify regions of the parameter space where high- T_c superconductivity might be expected at higher values of the coupling U . Our results fix errors in and reconcile previous studies as well as provide more detail on the structure of the order parameter in a wider range of parameters, thereby serving as solid grounds for benchmarking of new nonperturbative methods. Since obtaining controlled numeric results at essentially nonzero values of U is extremely computationally expensive, our work provides a valuable guide for such studies in the search for high- T_c superconductivity in the Hubbard model.

The paper is organized as follows: In Sec. II A we review the method for obtaining the phase diagram by tracing the development of instability in each particular channel. Section II B presents a brief overview of the symmetry adapted basis states on the square lattice. Section II C addresses competition between magnetic and superconducting instabilities along the line in the (t', n) plane where the Van Hove singularity is at the Fermi surface. We present the obtained phase diagram in Sec. III A and discuss the behavior of the effective coupling strength in the Cooper channel, which controls the superfluid T_c , in Sec. III B. In Sec. III C we compare our results to previous work, while Sec. IV gives general concluding remarks.

II. METHOD

A. Perturbative treatment of the Fermi liquid

Our derivations follow the standard perturbative approach, adopted, e.g., in Refs. [24,25]. The dispersion relation on the square lattice reads (k_x and k_y are the momentum components

of \mathbf{k})

$$\epsilon(\mathbf{k}) = -2t(\cos k_x + \cos k_y) + 4t' \cos k_x \cos k_y. \quad (2)$$

The Green's function $G(\mathbf{k}, \xi)$ can be obtained from the Dyson's equation

$$G(\mathbf{k}, \xi_n) = \frac{1}{i\xi_n - \epsilon(\mathbf{k}) + \mu - \Sigma(\mathbf{k}, \xi_n)}, \quad (3)$$

where μ is the chemical potential, $\xi_n = (2n + 1)\pi/\beta$ are the Matsubara frequencies, and $\Sigma(\mathbf{k}, \xi_n)$ is the self-energy (in the following we adopt the units of the hopping amplitude t).

In the weak-coupling limit at sufficiently low temperatures $T \ll E_F$ the system is a Fermi liquid with a well-defined Fermi surface. The quasiparticle Green's function in the vicinity of the Fermi surface $|\xi| \ll E_F$ and $|k - k_F(\hat{k})| \ll k_F(\hat{k})$ takes on the form:

$$G(\mathbf{k}, \xi) \equiv \frac{z(\hat{k})}{i\xi - \mathbf{v}_F(\hat{k}) \times [\mathbf{k} - \mathbf{k}_F(\hat{k})]}. \quad (4)$$

Here the Fermi surface is parametrized in terms of the Fermi momentum $\mathbf{k}_F(\hat{k})$ in the direction \hat{k} of the vector \mathbf{k} . Comparing Eqs. (3) and (4) we obtain the Fermi velocity $\mathbf{v}_F(\hat{k}) = z(\hat{k})\nabla_{\mathbf{k}_F}(\epsilon(\mathbf{k}_F) + \Sigma_R(\mathbf{k}_F, \xi_n))$ and the quasiparticle residue $z(\hat{k}) = (1 - \lim_{\xi_n \rightarrow 0} \frac{\Sigma_I(\mathbf{k}_F, \xi_n)}{\xi_n})^{-1}$.

As the temperature is lowered further, the development of the Cooper instability is marked by divergence of the pairing susceptibility at the critical temperature T_c , which is exponentially smaller than E_F .

The instability is due to weak attraction between fermions, which in our case is an emergent low-energy many-body property. Mathematically, the effective interaction is described by the irreducible in the particle-particle channel four-point vertex Γ^{pp} , which in general is a sum of all possible four-point diagrams that cannot be split into disconnected pieces by cutting two particle lines. The Cooper pairing susceptibility is proportional to the full effective vertex F^{pp} , which diverges at T_c and is related to Γ^{pp} via the Bethe-Salpeter equation shown diagrammatically in Fig. 1. From the Bethe-Salpeter equation we see that the smallness of the attractive part of Γ^{pp} is a natural condition preventing F^{pp} from dramatic growth at $T \ll E_F$. Indeed, in the FL regime, the leading contribution to the integral over \mathbf{k}_3 in the second term on the r.h.s. of Fig. 1 comes from the close vicinity to the Fermi surface,

$$\int d\mathbf{k}_3 \sum_{\xi_3} G(p_3)G(-p_3) \approx \ln \frac{cE_f}{T} \int \frac{ds}{2\pi} \frac{z^2(\hat{k})}{2\pi v_F}, \quad (5)$$

where ds is the Fermi surface element. Only the finite temperature (i.e., discreteness of Matsubara frequency ξ_3) prevents the integral in the r.h.s. from logarithmic divergence.

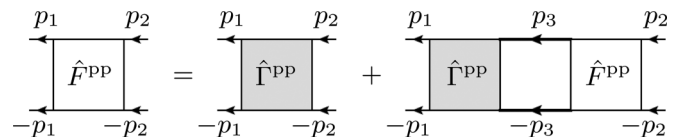


FIG. 1. The Bethe-Salpeter equation for Γ^{pp} with $p_i \equiv (\xi_i, \mathbf{k}_i)$. Summation over ξ_i and integration over \mathbf{k}_i is assumed.

With logarithmic accuracy at $T \ll E_F$, we have

$$F_{\hat{k}_1, \hat{k}_2}^{\text{pp}} \approx \Gamma_{\hat{k}_1, \hat{k}_2}^{\text{pp}} + \ln \frac{c E_f}{T} \int \Gamma_{\hat{k}_1, \hat{k}_3}^{\text{pp}} Q_{\hat{k}_3} F_{\hat{k}_3, \hat{k}_2}^{\text{pp}} d\hat{k}_3, \quad (6)$$

where $F_{\hat{k}_1, \hat{k}_2}$ and $\Gamma_{\hat{k}_1, \hat{k}_2}$ are F^{pp} and Γ^{pp} at vanishing frequencies projected to the Fermi surface:

$$F_{\hat{k}_1, \hat{k}_2}^{\text{pp}} \equiv F^{\text{pp}}(\mathbf{k}_1 = \mathbf{k}_F(\hat{k}_1), \xi_1 \rightarrow 0; \mathbf{k}_2 = \mathbf{k}_F(\hat{k}_2), \xi_2 \rightarrow 0) \quad (7)$$

and $Q_{\hat{k}}$ is the product of $z^2(\hat{k})$ and the density of states at the k point on the Fermi surface.

$$Q_{\hat{k}} = \frac{k_F(\hat{k}) z^2(\hat{k})}{2\pi v_F(\hat{k})} \quad (8)$$

Switching to matrix notations $F_{\hat{k}_1, \hat{k}_2}^{\text{pp}} \rightarrow \hat{F}^{\text{pp}}$, $\Gamma_{\hat{k}_1, \hat{k}_2}^{\text{pp}} \rightarrow \hat{\Gamma}^{\text{pp}}$, $Q_{\hat{k}_2} \rightarrow \hat{Q}$ we find

$$\hat{F}^{\text{pp}} \approx \left[1 - \ln \left(\frac{E_F}{T} \right) \hat{\Gamma}^{\text{pp}} \hat{Q} \right]^{-1} \hat{\Gamma}^{\text{pp}}, \quad (9)$$

implying that \hat{F}^{pp} , and thus the static response function in the Cooper channel, diverges at the critical temperature

$$T_c = c E_F e^{-1/\lambda}, \quad (10)$$

where λ is the largest positive eigenvalue of $\hat{\Gamma}^{\text{pp}} \hat{Q}$. Solving the problem with logarithmic accuracy (which is guaranteed in the $U \rightarrow 0$ limit due to $\lambda \rightarrow 0$ and the corresponding exponential smallness of T_c) amounts to finding the eigenvalues/eigenvectors of a real symmetric matrix

$$T_{\hat{k}_1, \hat{k}_2} \psi_{\hat{k}_2} = \lambda \psi_{\hat{k}_1}, \quad T_{\hat{k}_1, \hat{k}_2} = Q_{\hat{k}_1}^{\frac{1}{2}} \Gamma_{\hat{k}_1, \hat{k}_2} Q_{\hat{k}_2}^{\frac{1}{2}}, \quad (11)$$

where the eigenvector $\psi_{\hat{k}}$ is the wave function of the Cooper pair in the momentum representation.

The effective vertex $\hat{\Gamma}^{\text{pp}}$ can be computed as a diagrammatic expansion in the bare coupling U . In this expansion the first order diagram is a negative constant $-U$, which by itself can never lead to a diverging denominator in Eq. (9). The first nonvanishing contribution to Cooper pairing comes from the second order in the U diagram, shown in Fig. 2, which features nontrivial momentum dependence giving rise to positive eigenvalues of the matrix $T_{\hat{k}_1, \hat{k}_2} \psi_{\hat{k}_2}$. All the diagrams beyond second order are vanishing in the limit $U \rightarrow 0$ and can be neglected. With the same accuracy, the propagator lines in the diagram in Fig. 2 are given by the bare noninteracting Green's function G_0 , i.e., the self-energy contribution in Eq. (3) can be neglected giving

$$G_0(\mathbf{k}, \xi_n) = \frac{1}{i\xi_n - \epsilon(\mathbf{k}) + \mu}. \quad (12)$$

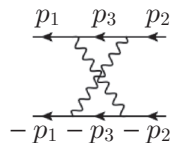


FIG. 2. The second-order diagram contributing to $\hat{\Gamma}^{\text{pp}}$. The wavy lines are the interaction vertices U , the straight lines with arrows are the noninteracting propagators G_0 . Integration over internal momenta is assumed.

Correspondingly, in Eq. (4), the quasiparticle residue $z(\hat{k}) = 1$. Thus, the diagram Fig. 2 is given by

$$\Gamma_{\hat{k}_1, \hat{k}_2} \approx \chi_{\hat{k}_1, \hat{k}_2}^{\text{ph}} = - \int \frac{d^d q}{(2\pi)^d} \frac{v(\epsilon(k+q)) - v(\epsilon(k))}{\epsilon(k+q) - \epsilon(k)}, \quad (13)$$

where $v(\epsilon) = [1 + \exp((\epsilon - \mu)/T)]^{-1}$ is the Fermi-Dirac distribution function. In two dimensions it is convenient to parametrize \hat{k} with the polar angle θ and to write the eigenvalue/eigenvector problem explicitly as

$$\int_0^{2\pi} \frac{d\theta}{2\pi} T_{\theta_1, \theta_2} \psi_{\theta_2} = g \psi_{\theta_1}, \quad T_{\theta_1, \theta_2} = Q_{\theta_1}^{\frac{1}{2}} \Gamma_{\theta_1, \theta_2} Q_{\theta_2}^{\frac{1}{2}}. \quad (14)$$

Note that this parametrization only works for connected Fermi surfaces, which is the case for all of parameter space in our model for values $t' \leq 0.5$.

We employ the following protocol to obtain the ground-state phase diagram:

- (1) For a given set of parameters (t', n) , the Fermi surface is found as the pole of G_0 , Eq. (12), in the limit $T \rightarrow 0$, which gives $v_F(\hat{k})$ and $k_F(\hat{k})$.
- (2) The matrix $\Gamma_{\theta_1, \theta_2}$ is computed using Eq. (13) by Monte Carlo numerical integration.
- (3) The eigenvalue problem, Eq. (14), is solved in the basis given by the point symmetry group (as explained below).
- (4) The largest eigenvalue λ and the corresponding eigenvector determines the superfluid ground state realized at the given set of parameters.

B. Classification of basis states on the square lattice

The symmetry operations on the square lattice form the point group D_4 (the two-dimensional point group corresponding to D_{4h}). The operations are the identity (E), two rotations by $\pm\pi/2$ (C_4) and one rotation by π (C_2) in the main symmetry axis (perpendicular to the plane) as well as two rotations by π around the horizontal/vertical in-plane axes (C'_2) and two π rotations around the diagonal in-plane axes (C''_2).

The D_4 symmetry dictates that the matrix $\Gamma_{\theta_1, \theta_2}$ splits into four independent singlet blocks, known as s , g , d_{xy} , and $d_{x^2-y^2}$, which correspond to one-dimensional irreducible representations A_1 , A_2 , B_1 , B_2 , and the doubly degenerate triplet block p , which corresponds to the two-dimensional irreducible representation E_1 . The E_1 sector further splits into p_x and p_y eigenvalues/eigenfunctions, which are related to each other by a $\pm\pi/2$ rotation. For each of the six sectors, the symmetry properties of the corresponding eigenvectors $\Psi(\theta)$ are readily seen from their Fourier expansions (with integer values of m):

$$A_1: \Psi_s(\theta) = \sum_{m=0}^{\infty} A_m \cos(4m\theta) \quad (15)$$

$$A_2: \Psi_g(\theta) = \sum_{m=0}^{\infty} B_m \sin((4m+4)\theta) \quad (16)$$

$$B_1: \Psi_{d_{xy}} = \sum_{m=0}^{\infty} C_m \cos((4m+2)\theta) \quad (17)$$

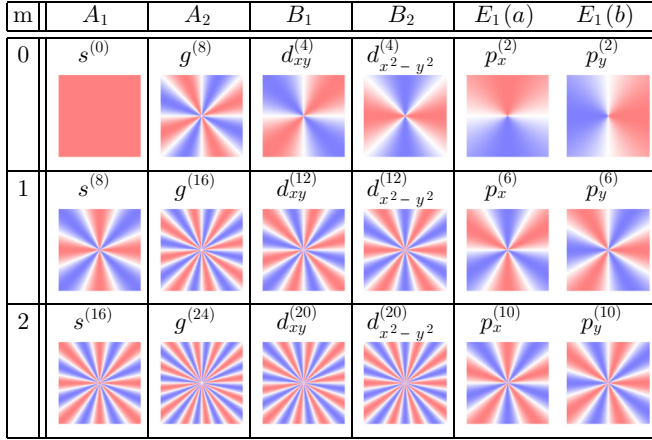


FIG. 3. The form of basis functions in the Brillouin zone (red, blue, and white colors correspond to positive values, negative values, and nodes respectively) categorized by irreducible representation and the order of harmonic m . [See Eqs. (15)–(19)].

$$B_2: \Psi_{d_{x^2-y^2}}(\theta) = \sum_{m=0}^{\infty} D_m \sin((4m+2)\theta) \quad (18)$$

$$E_1: \begin{cases} \Psi_{p_x}(\theta) = \sum_{m=0}^{\infty} E_m \cos((2m+1)\theta) \\ \Psi_{p_y}(\theta) = \sum_{m=0}^{\infty} E_m \sin((2m+1)\theta) \end{cases} \quad (19)$$

The eigenfunctions Ψ_s are invariant under all symmetry operations of the point group. The eigenfunctions Ψ_g are invariant under E , C_4 , and C_2 but change sign under C'_2 and C''_2 . Both $\Psi_{d_{xy}}$ and $\Psi_{d_{x^2-y^2}}$ change signs under C_4 , while only $\Psi_{d_{xy}}$ changes sign under C'_2 and only $\Psi_{d_{x^2-y^2}}$ changes sign under C''_2 . Finally Ψ_{p_x} and Ψ_{p_y} transform into each other under C_4 and into a linear combination thereof under all the other symmetry operations. We refer to the $m=0$ contribution to each eigenfunction in Eqs. (15)–(19) as the corresponding fundamental mode and all the eigenfunctions with $m>0$ as higher harmonics. We assign a number in the superscript to each eigenfunction, which signifies the amount of zeros of the function. An example of the fundamental mode and the first two higher harmonics projected onto the Brillouin zone of the square lattice is given in Fig. 3. It must be noted that identifying the largest coefficient in the expansion in Eqs. (15)–(19) for each eigenfunction is not always sufficient to classify the eigenfunction in terms of the number of nodes it features since the subleading components can have a significant net contribution that can change the nodal structure. We therefore classify each state in the phase diagram by explicitly counting the number of zeros in the eigenfunction that corresponds to the largest eigenvalue.

C. Instabilities along the Van Hove singularity line

In the weak-coupling limit, the superfluid phase is realized in the ground state in the whole parameter range with the exception of two points. Both of them lie on the line in the (t', n) plane where the density of states at the Fermi surface diverges due to the Van Hove singularity. This line (referred to as Van Hove line) is defined by the condition $\mu = 4t'$. At $t' = 0$ and $n = 1$, due to nesting of the Fermi surface with the momentum $\mathbf{Q}_{AFM} = (\pi, \pi)$, the spin ordering instability dominates, and

the ground state is an antiferromagnet. At $t' = 0.5$, $n = 0$ the ferromagnetic instability with the nesting vector $\mathbf{Q}_{FM} = (0, 0)$ is leading. Generally, along the line, the particle-hole susceptibility χ^{ph} diverges double logarithmically [69] at momentum transfer $\mathbf{Q} = (\pi, \pi)$ and logarithmically at $\mathbf{q} = (0, 0)$ as:

$$\chi^{\text{ph}}(\mathbf{q}) \sim \left(\frac{1}{2\pi^2} \right) \frac{1}{\sqrt{1-4t'^2}} \ln \left(\frac{1}{\Lambda} \right) \quad (20)$$

$$\chi^{\text{ph}}(\mathbf{Q}) \sim \left(\frac{1}{2\pi^2} \right) \ln(1 + \sqrt{1-4t'^2}) \ln \left(\frac{1}{\Lambda} \right), \quad (21)$$

where Λ is the infrared energy cutoff. The particle-particle susceptibility also diverges at \mathbf{q} and \mathbf{Q} :

$$\chi^{\text{pp}}(\mathbf{q}) \sim \left(\frac{1}{4\pi^2} \right) \frac{1}{\sqrt{1-4t'^2}} \ln^2 \left(\frac{1}{\Lambda} \right) \quad (22)$$

$$\chi^{\text{pp}}(\mathbf{Q}) \sim \left(\frac{1}{2\pi^2} \right) \frac{\tan^{-1} \left(\frac{2t'}{\sqrt{1-4t'^2}} \right)}{\sqrt{1-4t'^2}} \ln \left(\frac{1}{\Lambda} \right). \quad (23)$$

Since both particle-particle and particle-hole channels are divergent along the Van Hove line, the magnetic and superfluid instabilities fuel each other and a simple Bethe-Salpeter analysis is insufficient. The behavior in this regime has been extensively studied by means of RG [39] and parquet approximation [70]. In particular, it was shown that the $d_{x^2-y^2}^{(4)}$ state is dominant along the Van Hove line at small U . Larger values of U were also addressed in these studies, but the methods are not controlled there and exact results are still due. At hopping values $t' \geq 0.5$ another line of special interest exists, which is defined by the Van Hove singularity crossing the Fermi surface nested with the momentum $q = (k, k)$, $k = \pm \cos^{-1}(\frac{1}{2|t'|})$ [54]. The line starts from the ferromagnetic point and is given by the equation $\mu = -\frac{1}{t'}$. It appears that the physics in the vicinity of $t' = 0.5$, even for $t' \leq 0.5$, is largely influenced by this line (see below). Above this line there is a finite region where the Fermi surface has a Fermi pocket around $(k_x, k_y) = (0, 0)$. All the aforementioned lines as well as the corresponding Fermi surfaces for all regions within parameter space of $0 \leq n \leq 2$ and $0 \leq t' \leq 0.7$ are shown in Fig. 4.

III. RESULTS

A. Phase diagram

Our main result, the ground-state phase diagram in the $U \rightarrow 0$ limit for the range of density $0 < n < 2$ and the next-nearest-neighbor hopping amplitude $0 \leq t' \leq 0.5$, is presented in Fig. 5. The diagram turns out to be very rich with twelve different states, which we characterize by the number of nodes of the superfluid order parameter, realized with the corresponding symmetries of each of the five irreducible representations. Controlled results at essentially nonzero U for $t' = 0$ [60] suggest that phases with a high number of nodes, i.e., higher than that in the fundamental mode of the corresponding irreducible representation, tend to disappear as U is increased. In particular, the authors demonstrate that the $p^{(6)}$ phase, which occupies a significant region in the $U \rightarrow 0$ limit (seen in Fig. 5 at $t' = 0$, $n \sim 0.6$) vanishes already at $U = 0.08$. Therefore, it is possible that this diversity of phases

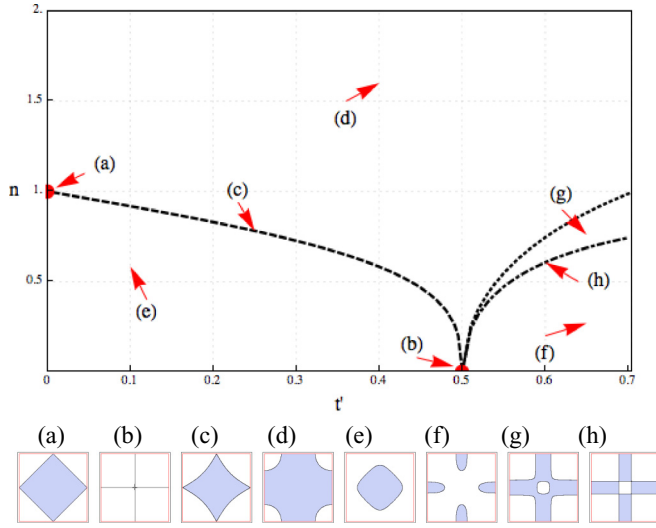


FIG. 4. The change of Fermi surface topology in the range of parameters $0 \leq n \leq 2$ and $0 \leq t' \leq 0.7$. The Van Hove line (dashed), second line of nesting (dot-dashed), and line beneath which a Fermi pocket exists (dotted) are plotted; see text for definitions of the lines. Characteristic Fermi surfaces in the first Brillouin zone ($k_x, k_y \in [-\pi, \pi)$) are shown for specific points in the parameter space: (a) the antiferromagnetic point $\{n = 1, t' = 0\}$, (b) the ferromagnetic point $\{n = 0, t' = 0.5\}$, (c) an arbitrary point along the Van Hove line $\{n = 0.78, t' = 0.25\}$, (d) above the Van Hove line $\{n = 1.60, t' = 0.4\}$, (e) below the Van Hove line $\{n = 0.58, t' = 0.1\}$, (f) below the second line of nesting $\{n = 0.27, t' = 0.65\}$, (g) above the second line of nesting $\{n = 0.76, t' = 0.65\}$, in the region where a Fermi pocket exists around $(k_x, k_y) = (0, 0)$, (h) on the second line of nesting $\{n = 0.61, t' = 0.6\}$.

and especially the presence of higher-harmonic states may be a weak-coupling limit artifact. We only study positive values of t' , since for $t' < 0$ the phase diagram is obtained by reflection symmetry about the point $(t' = 0, n = 1)$, which is due to the mapping of the Hamiltonian onto itself upon replacing all the particles with holes.

To obtain the phase diagram in Fig. 5, we introduce a grid in the (t', n) plane and find the leading instability by the approach described in Secs. II A–II B at each point of the grid. The horizontal grid step is $\Delta_{t'} = 0.025$ in regions with multiple phase boundaries in close proximity and $\Delta_{t'} = 0.05$ everywhere else. The vertical grid step is $\Delta_n = 0.05$ everywhere, except in the vicinity of the Van Hove line, where results for densities $n_{VH} \pm 0.001$ were obtained. This high resolution, which required a substantial computational effort, was necessary to obtain a reliable phase diagram that can be used as a benchmark for further investigations.

Clearly, the region beneath half filling ($n = 1$) is far richer than the region above. This can be related to the presence of the Van Hove line in that part of the diagram. Indeed, most higher-order harmonics are to be found in the vicinity of this line. All irreducible representations have at least one higher-order wave realized over a finite region of the phase diagram. These are, with the exception of E_1 , only small regions, mostly at the borders between two or more phases belonging to different irreducible representations. White regions are due to very small values of λ ($< 10^{-6}$) at which it is difficult to

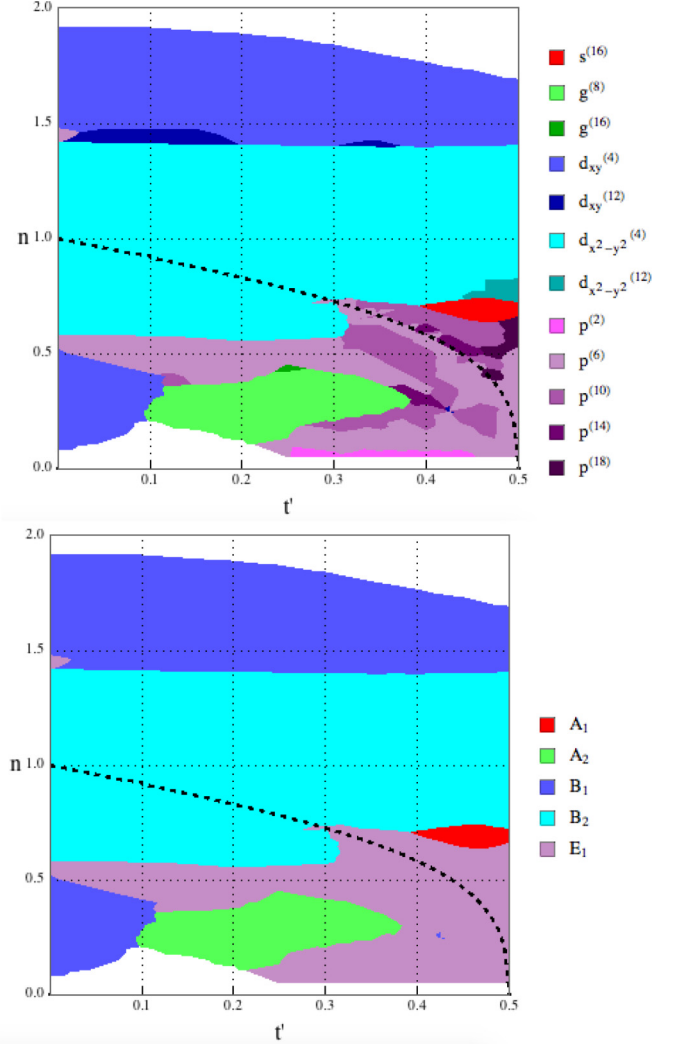


FIG. 5. top: Phase diagram for the parameter range of $0 < n < 2$ and $0 < t' < 0.5$. bottom: same parameter range by leading irreducible representation. The presence of a Van Hove singularity is portrayed by the black dashed line.

reliably claim which phase is realized. These regions, however, are not immediately relevant for future studies of high- T_c superconductivity.

In the following, we discuss the phases classified by their symmetries corresponding to each of the irreducible representations:

A₁: The contribution of the fundamental mode $s^{(0)}$ to the vertex Γ^{PP} is negative [71–73], and therefore there is no Cooper instability in the lowest-order s -wave channel. Higher harmonics, on the other hand, have positive eigenvalues and the corresponding phases are realized over some regions of the parameter space. In particular, it may appear surprising that the $s^{(16)}$ harmonic is dominant in a finite region around $t' = 0.5$ and $n = 0.7$ over the lower-order $s^{(8)}$ harmonic. This may be due to the presence of a second nested line at $t' > 0.5$.

A₂: The $g^{(8)}$ harmonic dominates at low fillings ($n < 0.5$) and intermediate values of hopping ($0.1 < t' < 0.4$). A small region of the $g^{(16)}$ harmonic was found around $t' = 0.25$ and $n = 0.45$. This is a region on the border between the $g^{(8)}$ and

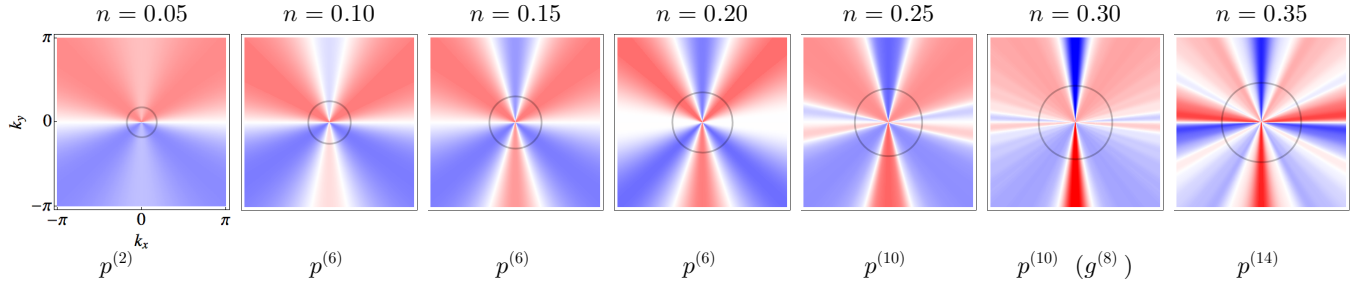


FIG. 6. The transition between the first four waves of the E_1 irreducible representation are seen along the line of $0.05 \leq n \leq 0.35$ at $t' = 0.375$. The type of wave is identified below each figure. It has to be noted that at the point at $n = 0.30$ the leading wave is $g^{(8)}$, however we have decided to include the point for completeness reasons. Individual Fermi surfaces are drawn in black.

$p^{(6)}$ phases and might also be influenced by the $d_{x^2-y^2}^{(4)}$ region at higher doping values. It is thus most likely realized as a frustrated intermediate state on the crossover between those phases.

B₁: A similar scenario happens at the crossover between $d_{x^2-y^2}^{(4)}$ and $d_{xy}^{(4)}$ regions at $n = 1.45$: The crossover between the two is via a strip of the $d_{xy}^{(12)}$ phase. It is interesting to note that the boundary between $d_{x^2-y^2}^{(4)}$ and $d_{xy}^{(4)}$ appears at essentially the same doping independent of the value of t' . This happens mainly because the shape of the Fermi surface at high values of doping is only weakly dependent on the hopping amplitude. Except for the region of high doping $n > 1.45$, another region of $d_{xy}^{(4)}$ exists at small values of $t' < 0.15$ and fillings $n < 0.55$, which is essentially a continuation of the first region reflected at the symmetry point of the phase diagram. Finally a tiny region of $d_{xy}^{(12)}$ was found at $t' = 0.475$ and $n = 0.25$ inside of a region dominated by the E_1 irreducible representation. It seems to be a consequence of frustration between $p^{(6)}$, $p^{(10)}$, and $p^{(14)}$ as it sits exactly at the boundary between those phases. It is possible that there are multiple such tiny regions spread over the phase diagram that are below our resolution.

B₂: The $d_{x^2-y^2}^{(4)}$ state dominates in a wide region around half filling. A relatively small region of the $d_{x^2-y^2}^{(12)}$ state was found on the boundary between $d_{x^2-y^2}^{(4)}$ and $s^{(16)}$. Similarly to the case of $s^{(16)}$, we attribute the existence of this $d_{x^2-y^2}^{(12)}$ phase to the proximity to the line of Fermi surface nesting at $t' > 0.5$ discussed above.

E₁: This irreducible representation displays the richest variety of phases as all first five p -type waves are realized in the phase diagram. However, apart from a few exceptions, the geometry of the order parameter is not highly symmetric, compared to examples of p waves in Fig. 3, and some of the nodes are separated by only small intervals. This often happens to a degree where it is difficult to identify the exact number of nodes and the crossovers between the corresponding states. The dominant wave in most regions is either $p^{(6)}$ or $p^{(10)}$, and not the fundamental $p^{(2)}$ harmonic, which can be found only in the low density regions. It seems that the E_1 phase has the tendency to go towards the $p^{(2)}$ harmonic as $n \rightarrow 0$. Whether this is true for all values of t' within the E_1 region is unclear as in practice we have only computed the leading instability down to $n = 0.05$ which is the minimal value of density within our resolution.

We see that at low values of t' the $p^{(6)}$ state dominates with the exception of a small region of $p^{(10)}$ on the boundary of $g^{(8)}$ and $d_{xy}^{(4)}$. Another region of the $p^{(6)}$ phase is at relatively low fillings $0.1 < n < 0.25$ and $t' > 0.2$. It transitions smoothly into $p^{(10)}$, then turns into $p^{(14)}$ at values of around $n \sim 0.3$. As a typical example, we show the transformation of the p -wave order parameter at a fixed $t' = 0.375$ as the density is increased from 0.05 to 0.35 in Fig. 6.

As one approaches the Van Hove line at yet higher values of doping and t' the phase diagram becomes patched with both $p^{(6)}$ and $p^{(10)}$ regions present. Interestingly, just below the Van Hove line the $p^{(6)}$ phase becomes clearly dominant again. Above the line there are multiple E_1 regions, with $p^{(10)}$ up to about $t' > 0.38$, followed by a region of $p^{(14)}$, a small region of $p^{(18)}$, and, finally, again $p^{(6)}$ as the line approaches the FM point at $t' \geq 0.47$. Also, at values of $t' > 0.4$ and around quarter filling we obtain regions of the high harmonic $p^{(18)}$, similarly to other high-order phases realized in the region ($s^{(16)}$ and $d_{x^2-y^2}^{(12)}$). We suspect that the high order of the leading harmonic is influenced by the aforementioned line of nesting at $t' \geq 0.5$.

Along the Van Hove line it is possible to identify a separation between regions influenced by the FM and AFM points. Close to the AFM point the singlet $d_{x^2-y^2}^{(4)}$ phase dominates as it corresponds to the symmetry of the AFM-type spin configuration. In the vicinity of the FM point the triplet $p^{(6)}$ phase dominates corresponding to the symmetry of the FM configuration. The respective boundary between B_2 and E_1 has been analytically calculated to be at $t' = 2/e \approx 0.184$ in Ref. [25]. We identified the leading phase to be $p^{(6)}$ for values $t' \geq 0.285$. For smaller values of t' the region of densities where $p^{(6)}$ dominates must be too small to be captured within our resolution. It is also worth noting that even close to the FM point $p^{(6)}$ is the leading state instead of $p^{(2)}$.

B. Effective coupling strength

The value of the highest effective coupling strength across the parameter space, irrespective of the irreducible representation it belongs to, is plotted in Fig. 7. There are two maxima around the FM and AFM points. The peak at the FM point is sharper than at the AFM point. This is due to the fact that both the particle-hole susceptibility χ^{ph} [Eq. (13)] and the density of states diverge at the same vector $q = (0,0)$. However, this does not immediately imply that the critical temperature is also

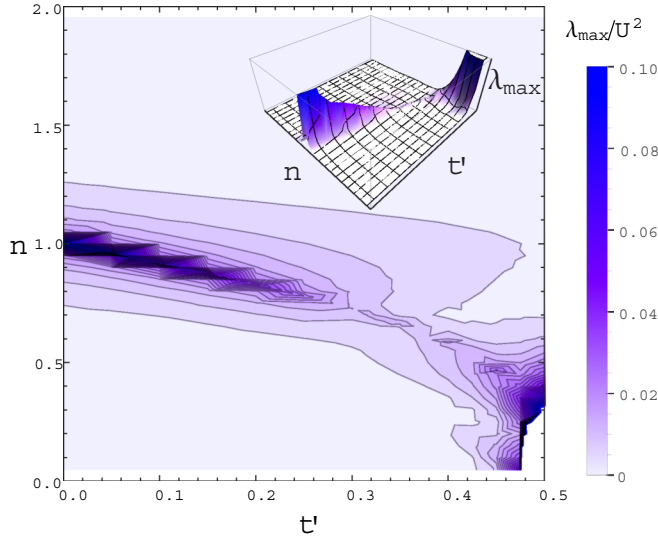


FIG. 7. Plot of highest effective coupling constant λ_{\max} irrespective of type of wave. Inset shows a 3D version of the same plot. Clear maxima can be seen at the FM and AFM point as well as an increase in coupling strength in the vicinity of the Van Hove line.

high in this regime—at low fillings T_c actually becomes low due to the lattice system approaching the continuum limit with a small value of E_F .

Interestingly, at $t' = 0.5$ the effective coupling constant is relatively large close to quarter filling $n = 0.5$. This is due to the presence of the line of Van Hove singularity passing through this point at higher next-nearest-neighbor hopping parameters ($t' > 0.5$), as mentioned earlier. As an illustration, we computed the effective coupling strength at two points outside of our range of parameters close to this line at $t' = 0.55$ and $n = \{0.55, 0.60\}$ obtaining $\lambda = \{0.062, 0.0218\}$, respectively, which demonstrates the rapid growth of the effective coupling on approach to the nested point $t' = 0.5, n = 0.5$. To show that at $t' = 0.5$ the magnitude of λ is comparable to that in the region around the AFM point we have calculated two points at $t' = \{0.55, 0.60\}$ with $\lambda/U^2 = \{0.0620, 0.0218\}$, respectively. We found that the effective coupling around $t' = 0.5, n = 0.5$ is comparable to the values near the AFM point (to be compared with $\lambda/U^2 = 0.0481$ at $t' = 0.01, n = 1.0$). A substantial increase in the leading λ is seen in the vicinity of the whole Van Hove line. This effect is strongest close to points with nesting, but can be observed even at intermediate values of t' .

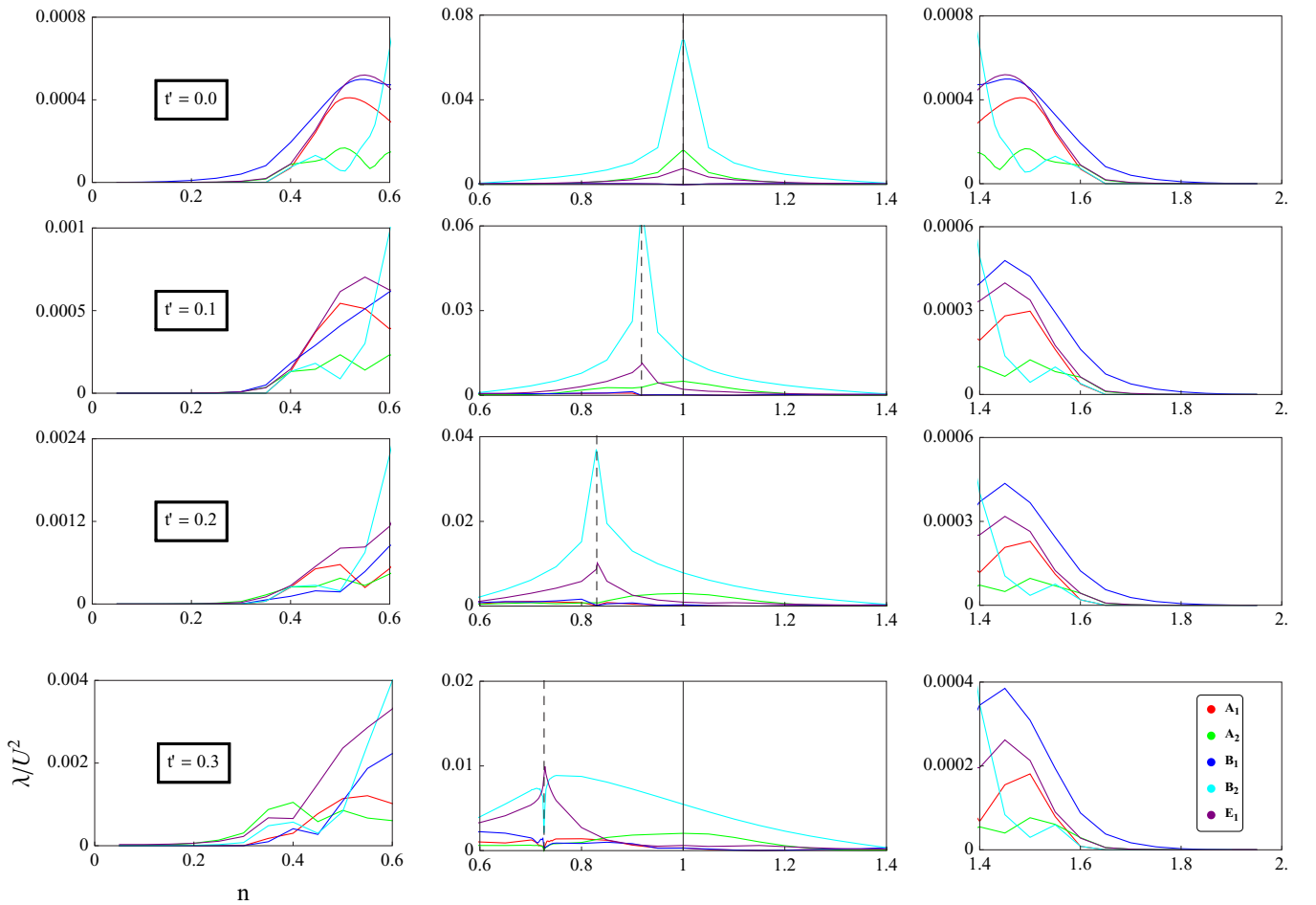


FIG. 8. The leading eigenvalue for each of the irreducible representations is given as a function of n at $t' = \{0.0, 0.1, 0.2, 0.3\}$. Dashed lines correspond to Van Hove densities at $n_{VH} = \{1.0, 0.918, 0.830, 0.726\}$, respectively. The closest measurements to the Van Hove points were performed at $n_{VH} \pm 0.001$.

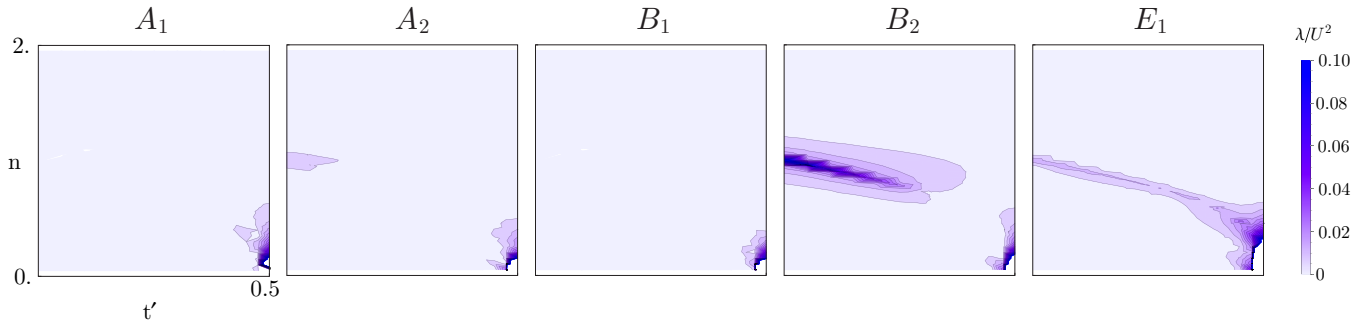


FIG. 9. The leading effective coupling constant λ for each of the irreducible representations. From left to right: A_1 , A_2 , B_1 , B_2 , E_1 . One can see that the AFM point does not affect the effective coupling of A_1 and B_1 representations, while the FM point seems to affect all waves alike. A clear increase in λ for E_1 can only be seen along the Van Hove line, while for $d_{x^2-y^2}^{(4)}$ the coupling strength dies out along the Van Hove line away from the AFM point.

In Fig. 8 we plot the leading eigenvalues by irreducible representation for $t' = \{0, 0.1, 0.2, 0.3\}$ as a function of density n . The maximal values for λ correspond to the Van Hove densities, located at $n_{VH} = \{1, 0.918, 0.830, 0.726\}$, respectively.

In Fig. 9, we show contour maps of the leading eigenvalue for each of the irreducible representations in the whole range of parameters. Near the AFM point only B_2 harmonics see a drastic increase in the effective coupling strength, whilst there is also a slight increase observed for A_2 . In contrast, the coupling strength for A_1 and B_1 exhibits a drop near the AFM point. The E_1 harmonics have a relatively high eigenvalue along the whole Van Hove line. A clear increase in coupling strength for all representations near the FM point is observed, which spreads for all the representations except B_1 up to quarter filling ($n = 0.5$) at $t' = 0.5$.

C. Comparison to previous work

Reference [24] has presented a weak-coupling phase diagram in a somewhat smaller range of parameters, where the phases are distinguished by their symmetry in terms of the irreducible representations without details of the nodal structure of the order parameter. Our results in Fig. 5 (bottom) are mostly consistent with Ref. [24]. The main difference is the B_1 phase ($d_{xy}^{(12)}$ harmonic) which we find inside the E_1 dominated region at $t' = 0.475$ and $n = 0.25$, and which is absent in Ref. [24]. Also, there are two small regions mentioned in Ref. [24]—for which the exact positions and extent were not provided—which we were not able to confirm within our resolution. These are a B_1 -type phase close to the $s^{(16)}/E_1$ boundary and an E_1 -type phase close to the $d_{xy}^{(4)}/g^{(8)}$. It is possible that multiple other tiny phases of this type might exist throughout the phase diagram, yet they would prove extremely difficult to capture.

At the level of differentiating between particular harmonics within each irreducible representation the phase diagram becomes far richer. We stress the importance of including high-order harmonics in the analysis because phases of a particular symmetry can be seen to be dominant only at a high expansion order in Eqs. (15)–(19). In particular, the previously overlooked B_1 -type phase, which is found between multiple higher harmonics of the E_1 -type phase, is realized as $d_{xy}^{(12)}$. Similarly, the $p^{(6)}$ phase at $t' = 0$ was overlooked in Ref. [25]

due to a low number of harmonics allowed in the analysis, but was found in this work as well as in Ref. [24] and is consistent with recently obtained controlled results at essentially finite U [60].

The only other analysis of the effective coupling strength was presented is Ref. [25]. In particular, the paper shows a plot of V_{eff} —which corresponds to λ divided by the density of states (ρ)—as a function of density n at $t' = 0$ and $t' = 0.3$. Figures in Ref. [25] obtain qualitatively similar results to Fig. 8, however it appears that the values for V_{eff} in Ref. [25] are missing a factor of density of states, which essentially changes the result. In fact, we were able to exactly reproduce Fig. 4 of Ref. [25] by deliberately dividing λ from our calculation by the density of states *twice*. This mistake overestimated the effective coupling strength in Ref. [25] by a factor of ~ 40 close to half filling (and by a factor ~ 20 compared to the maximum λ that we found at the Van Hove filling). Moreover, the $g^{(8)}$ and $p^{(2)}$ states are missing altogether in Figs. 2 and 4 of Ref. [25] despite being the leading instabilities at particular densities n .

IV. CONCLUSIONS

We have performed a perturbative analysis of the repulsive single-band Hubbard model with next-nearest-neighbor hopping t' , addressing the Cooper-pairing instability in the Fermi liquid regime in a wide range of t' and density n . Our results are asymptotically exact within the given resolution in the limit $U \rightarrow 0$. We have obtained the ground-state phase diagram and classified phases by their symmetry in terms of the corresponding irreducible representation as well as the nodal structure of the gap function, which resulted in a far richer phase diagram compared to previous works. We have also performed an analysis of the effective coupling strength in the Cooper channel, which controls the superfluid critical temperature. We have observed that the divergence of the density of states at the Fermi surface due to the Van Hove singularity has an influence on both the type of realized superfluid order as well as the effective interaction strength. Besides the widely discussed region near the AFM point, we have identified another region with high effective coupling around quarter filling $n = 0.5$ and $t' = 0.5$, which most likely extends to higher values of t' . This suggests that a detailed study of the model at higher values of next-nearest-neighbor

hoppings is of substantial interest in the context of high- T_c superconductivity. In general the phase diagram enables further work to start from intuition about the location and extent of regions with high effective coupling. Potentially, the Fermi-Hubbard model with next-nearest-neighbor hopping could be realized experimentally in optical lattices—as has been done with multiple other extended Hubbard models [74]—and provide actual transition temperatures values. Importantly, our results enable us to identify and correct some of the mistakes of previous works. Our work can serve as a solid foundation for application of accurate advanced methods to the model at essentially finite values of coupling U . The provided results can be used as a starting point for the construction of a phase diagram in the (n, t', U) parameter space. Instead of calculating a computationally expensive grid of points it is possible to follow individual phase transition lines to higher values of coupling U , as has been done at $t' = 0$ by Deng *et al.* [60]. It has to be noted that the landscape of the diagram might change

dramatically for nonvanishing values of U , and especially higher harmonics, which exist on the boundary between phases belonging to different irreducible representations, are likely to disappear as it happened for the $p^{(6)}$ harmonic at $t' = 0$, which vanished at $U = 0.08$.

ACKNOWLEDGMENTS

We are grateful to S. Raghu and A. Rømer for elaborating on and discussing details of their preceding results. We also thank N. Prokofiev, B. Svistunov, A. Chubukov, and S. Nikolaev for fruitful discussions. This work was supported by the Simons Collaboration on the Many Electron Problem, National Science Foundation under the Grant No. PHY-1314735. Y.D. and X.W.L. thank the support of the National Natural Science Foundation of China under Grant No. 11275185 and the Fundamental Research Funds for the Central Universities under Grant No. 2340000034.

-
- [1] J. Hubbard, *Proc. R. Soc. London A* **276**, 238 (1963).
 - [2] P. W. Anderson, *Science* **235**, 1196 (1987).
 - [3] P. W. Anderson *et al.*, *The Theory of Superconductivity in the High- T_c Cuprate Superconductors* (Princeton University Press, Princeton, NJ, 1997), Vol. 446.
 - [4] K. Miyake, S. Schmitt-Rink, and C. Varma, *Phys. Rev. B* **34**, 6554(R) (1986).
 - [5] M. Béal-Monod, C. Bourbonnais, and V. Emery, *Phys. Rev. B* **34**, 7716 (1986).
 - [6] D. J. Scalapino, E. Loh, Jr, and J. E. Hirsch, *Phys. Rev. B* **34**, 8190(R) (1986).
 - [7] D. Scalapino, *J. Low Temp. Phys.* **117**, 179 (1999).
 - [8] U. Schneider, L. Hackermüller, S. Will, T. Best, I. Bloch, T. Costi, R. Helmes, D. Rasch, and A. Rosch, *Science* **322**, 1520 (2008).
 - [9] M. Köhl, H. Moritz, T. Stöferle, K. Günter, and T. Esslinger, *Phys. Rev. Lett.* **94**, 080403 (2005).
 - [10] R. Jördens, N. Strohmaier, K. Günter, H. Moritz, and T. Esslinger, *Nature (London)* **455**, 204 (2008).
 - [11] Schneider *et al.*, *Nat. Phys.* **8**, 213 (2012).
 - [12] W. S. Bakr, J. I. Gillen, A. Peng, S. Fölling, and M. Greiner, *Nature (London)* **462**, 74 (2009).
 - [13] W. Hofstetter, J. I. Cirac, P. Zoller, E. Demler, and M. D. Lukin, *Phys. Rev. Lett.* **89**, 220407 (2002).
 - [14] R. Jördens *et al.*, *Phys. Rev. Lett.* **104**, 180401 (2010).
 - [15] B. Sriram Shastry, *Phys. Rev. Lett.* **56**, 2453 (1986).
 - [16] E. H. Lieb and F. Y. Wu, *Phys. Rev. Lett.* **20**, 1445 (1968).
 - [17] W. Kohn and J. Luttinger, *Phys. Rev. Lett.* **15**, 524 (1965).
 - [18] M. Baranov and M. Y. Kagan, *Z. Phys. B Condens. Matter* **86**, 237 (1992).
 - [19] M. Baranov, A. Chubukov, and M. Yu. Kagan, *Int. J. Mod. Phys. B* **6**, 2471 (1992).
 - [20] M. Y. Kagan and A. V. Chubukov, *Pis'ma Zh. Eksp. Teor. Fiz.* **50**, 483 (1989) [*JETP Lett.* **50**, 517 (1989)].
 - [21] A. V. Chubukov and J. P. Lu, *Phys. Rev. B* **46**, 11163 (1992).
 - [22] A. V. Chubukov, *Phys. Rev. B* **48**, 1097 (1993).
 - [23] H. Fukazawa and K. Yamada, *J. Phys. Soc. Jpn.* **71**, 1541 (2002).
 - [24] R. Hlubina, *Phys. Rev. B* **59**, 9600 (1999).
 - [25] S. Raghu, S. A. Kivelson, and D. A. Scalapino, *Phys. Rev. B* **81**, 224505 (2010).
 - [26] M. Salmhofer, *Commun. Math. Phys.* **194**, 249 (1998).
 - [27] B. Binz, D. Baeriswyl, and B. Douçot, *Ann. Phys.* **12**, 704 (2003).
 - [28] M. Salmhofer and C. Honerkamp, *Prog. Theor. Phys.* **105**, 1 (2001).
 - [29] C. Honerkamp and M. Salmhofer, *Phys. Rev. Lett.* **87**, 187004 (2001).
 - [30] J. Reiss, D. Rohe, and W. Metzner, *Phys. Rev. B* **75**, 075110 (2007).
 - [31] H. Zhai, F. Wang, and D.-H. Lee, *Phys. Rev. B* **80**, 064517 (2009).
 - [32] R. Shankar, *Rev. Mod. Phys.* **66**, 129 (1994).
 - [33] J. Polchinski, *arXiv:hep-th/9210046*.
 - [34] I. E. Dzyaloshinskii, *Zh. Eksp. Teor. Fiz.* **93**, 1487 (1987) [*Sov. Phys. JETP* **66**, 848 (1987)].
 - [35] H. Schulz, *Europhys. Lett.* **4**, 609 (1987).
 - [36] P. Lederer, G. Montambaux, and D. Poilblanc, *J. Phys.* **48**, 1613 (1987).
 - [37] D. Zanchi and H. Schulz, *Phys. Rev. B* **54**, 9509 (1996).
 - [38] A. T. Zheleznyak, V. M. Yakovenko, and I. E. Dzyaloshinskii, *Phys. Rev. B* **55**, 3200 (1997).
 - [39] D. Zanchi and H. J. Schulz, *Phys. Rev. B* **61**, 13609 (2000).
 - [40] A. A. Katanin and A. P. Kampf, *Phys. Rev. B* **68**, 195101 (2003).
 - [41] A. Neumayr and W. Metzner, *Phys. Rev. B* **67**, 035112 (2003).
 - [42] I. Khavkine, C.-H. Chung, V. Oganesyan, and H.-Y. Kee, *Phys. Rev. B* **70**, 155110 (2004).
 - [43] H. Yamase, V. Oganesyan, and W. Metzner, *Phys. Rev. B* **72**, 035114 (2005).
 - [44] H.-Y. Kee and Y. B. Kim, *Phys. Rev. B* **71**, 184402 (2005).
 - [45] C. J. Halboth and W. Metzner, *Phys. Rev. Lett.* **85**, 5162 (2000).
 - [46] C. Honerkamp, M. Salmhofer, N. Furukawa, and T. M. Rice, *Phys. Rev. B* **63**, 035109 (2001).
 - [47] C. Honerkamp, M. Salmhofer, and T. Rice, *Eur. Phys. J. B* **27**, 127 (2002).
 - [48] V. Hankevych, I. Grote, and F. Wegner, *Phys. Rev. B* **66**, 094516 (2002).
 - [49] V. Hankevych and F. Wegner, *Eur. Phys. J. B* **31**, 333 (2003).

- [50] V. Hankevych, B. Kyung, and A.-M. S. Tremblay, *Phys. Rev. B* **68**, 214405 (2003).
- [51] C. Husemann and M. Salmhofer, *Phys. Rev. B* **79**, 195125 (2009).
- [52] X. Chen, J. P. F. LeBlanc, and E. Gull, *Phys. Rev. Lett.* **115**, 116402 (2015).
- [53] A. Eberlein and W. Metzner, *Phys. Rev. B* **89**, 035126 (2014).
- [54] A. T. Rømer, A. Kreisel, I. Eremin, M. A. Malakhov, T. A. Maier, P. J. Hirschfeld, and B. M. Andersen, *Phys. Rev. B* **92**, 104505 (2015).
- [55] A. Luther, *Phys. Rev. B* **50**, 11446 (1994).
- [56] J. O. Fjærestad, A. Sudbø, and A. Luther, *Phys. Rev. B* **60**, 13361 (1999).
- [57] L. Balents and M. P. Fisher, *Phys. Rev. B* **53**, 12133 (1996).
- [58] H.-H. Lin, L. Balents, and M. P. A. Fisher, *Phys. Rev. B* **58**, 1794 (1998).
- [59] I. Dimov, P. Goswami, X. Jia, and S. Chakravarty, *Phys. Rev. B* **78**, 134529 (2008).
- [60] Y. Deng, E. Kozik, N. V. Prokof'ev, and B. V. Svistunov, *Europhys. Lett.* **110**, 57001 (2015).
- [61] R. Blankenbecler, D. J. Scalapino, and R. L. Sugar, *Phys. Rev. D* **24**, 2278 (1981).
- [62] R. Staudt, M. Dzierzawa, and A. Muramatsu, *Eur. Phys. J. B* **17**, 411 (2000).
- [63] E. Kozik, E. Burovski, V. W. Scarola, and M. Troyer, *Phys. Rev. B* **87**, 205102 (2013).
- [64] E. Gull, O. Parcollet, and A. J. Millis, *Phys. Rev. Lett.* **110**, 216405 (2013).
- [65] P. Staar, T. Maier, and T. C. Schulthess, *Phys. Rev. B* **89**, 195133 (2014).
- [66] B.-X. Zheng and G. K. Chan, *Phys. Rev. B* **93**, 035126 (2016).
- [67] J. LeBlanc, A. E. Antipov, F. Becca, I. W. Bulik, G. K. Chan, C.-M. Chung, Y. Deng, M. Ferrero, T. M. Henderson, C. A. Jiménez-Hoyos *et al.*, *Phys. Rev. X* **5**, 041041 (2015).
- [68] Z. Y. Meng, F. Yang, K.-S. Chen, H. Yao, and H.-Y. Kee, *Phys. Rev. B* **91**, 184509 (2015).
- [69] R. Hlubina, S. Sorella, and F. Guinea, *Phys. Rev. Lett.* **78**, 1343 (1997).
- [70] V. Y. Irkhin, A. Katanin, and M. Katsnelson, *Phys. Rev. B* **64**, 165107 (2001).
- [71] K. Brueckner, T. Soda, P. W. Anderson, and P. Morel, *Phys. Rev.* **118**, 1442 (1960).
- [72] L. P. Pitaevskii, *Sov. Phys. JETP* **10**, 1267 (1960).
- [73] V. Emery and A. Sessler, *Phys. Rev.* **119**, 43 (1960).
- [74] O. Dutta, M. Gajda, P. Hauke, M. Lewenstein, D.-S. Lühmann, B. A. Malomed, T. Sowiński, and J. Zakrzewski, *Rep. Prog. Phys.* **78**, 066001 (2015).